Determination of Fe3+/ΣFe of olivine-hosted melt inclusions using Mössbauer and XANES spectroscopy

M. Gaborieau, M. Laubier, N. Bolfan-Casanova, C.A. A Mccammon, D. Vantelon, A.I. I Chumakov, F. Schiavi, D.R. R Neuville, S. Venugopal

$Fe^{3+}/\Sigma Fe$ of olivine-hosted melt inclusions inferred from Mössbauer and XANES spectroscopy

M. Gaborieau[1*], M. Laubier[1], N. Bolfan-Casanova[1], C. McCammon[2], D. Vantelon[3], A.I. Chumakov[4], F. Schiavi[1], D. R. Neuville[5], S. Venugopal[1, 6]

[1]Université Clermont Auvergne, CNRS, IRD, OPGC, Laboratoire Magmas et Volcans, F-63000 Clermont-Ferrand, France

[2]Bayerisches Geoinstitut, Universität Bayreuth, D-95440 Bayreuth, Germany

[3]Synchrotron SOLEIL, BP 48 91192 Gif-sur-Yvette, France

[4]ESRF-The European Synchrotron, CS40220, 38043 Grenoble Cedex 9, France

[5]Institut de physique du globe de Paris, 75238 Paris Cedex 5, France

[6]Centre for Natural Hazards Research, Department of Earth Sciences, Simon Fraser University, BC, V5A 1S6, Canada

[*]Correspondence: marion.gaborieau@uca.fr

Declarations of interest: none

Keywords: beam damage, oxygen fugacity, arc magma, synchrotron Mössbauer, melt inclusion, XANES

Iron speciation is linked to the oxygen fugacity of the system; hence determining the $Fe^{3+}/\Sigma Fe$ ratio of glasses can allow us to determine their oxidation state. Using X-ray Absorption Near Edge Structure (XANES) spectroscopy in silicate glasses and olivine-hosted melt inclusions, previous studies have shown that arc basalts are more oxidized than mid-oceanic ridge basalts (MORB) and oceanic island basalts (OIB). However, Cottrell et al. (2018) have recently demonstrated that hydrous glasses can be affected by beam-induced oxidation

during XANES analysis, which leads to an over-estimation of their $Fe^{3+}/\Sigma Fe$ ratios. Here, we determined $Fe^{3+}/\Sigma Fe$ ratios in olivine-hosted melt inclusions from various arcs, MORB and OIB localities by Mössbauer and XANES spectroscopy. A careful evaluation of beam damage during XANES analysis was carried out with attentive investigation of XANES spectra and time series collected on hydrous basaltic and basanitic glasses using different radiation doses. Therefore, the $Fe^{3+}/\Sigma Fe$ ratios obtained with these two methods on the same sample set allowed us to constrain the oxidation state of those magmas by avoiding the effect of beam-induced oxidation that may occur during XANES analysis.

Our results show that melt inclusions from MORBs, OIBs and arc basalts display mean $Fe^{3+}/\Sigma Fe$ ratios of 0.10 ± 0.05 (n=5), 0.13 ± 0.05 (n=2) and 0.25 ± 0.15 (n=19), respectively. Mount Etna melt inclusions display a mean $Fe^{3+}/\Sigma Fe$ ratio of 0.26 ± 0.05 (n=7). Therefore, they confirm that arc magmas are more oxidized than those from hot spots and mid-ocean ridges. Furthermore, they suggest that the range in the oxidation state observed in our melt inclusion dataset may be linked to changes in the oxidation state of the mantle beneath arcs due to subduction processes.

1. Introduction

Many studies have demonstrated that arc basalts are more oxidized (~ QFM+1.5 ± 1; fO_2 given relatively to the quartz-fayalite-magnetite buffer; Gaillard et al. 2015 and references therein) than MORBs (QFM-1.2 to ~ QFM; e.g. Berry et al., 2018; Bézos and Humler, 2005; Birner et al, 2018; Christie et al., 1986; Cottrell and Kelley, 2011, 2013; Mallmann and O'Neill, 2009; O'Neill et al., 2018; H. L. Zhang et al., 2018). However, the oxidation state of the sub-arc mantle is still debated. Kelley and Cottrell (2009, 2012) and Brounce et al. (2014, 2015) suggest that variations in the $Fe^{3+}/\Sigma Fe$ ratio measured in basaltic glasses and olivine-hosted

melt inclusions from mid-ocean ridges and arcs can be explained by the sub-arc mantle being more oxidized than the mantle beneath ridges. On the other hand, Mallmann and O'Neill (2009) and Lee et al. (2005, 2010) proposed the use of other fO_2 proxies, namely V/Sc and Zn/ΣFe ratios in lavas and suggested that the oxidation state of the mantle wedge cannot be distinguished from that of the MORB mantle (see also Dauphas et al., 2009; Li and Lee, 2004).

Fe is an abundant multivalent 3d-transition element in silicate glasses, and its speciation is linked to the oxygen fugacity of the system (Kress and Carmichael, 1991). Many techniques allow measurements of the Fe oxidation state, such as wet chemistry (Bézos and Humler, 2005; Christie et al., 1986), Mössbauer spectroscopy (e.g. Jayasuriya et al., 2004; Mccammon, 2004; Partzsch et al., 2004; Zhang et al., 2018), the Flank method on the electron probe (e.g. Fialin et al., 2001; Zhang et al., 2018) and X-Ray absorption near-edge structure (XANES) spectroscopy. Micro-XANES has been widely used to provide $Fe^{3+}/\Sigma Fe$ in silicate glasses (e.g. Berry et al., 2003; Cottrell et al., 2009; Wilke et al., 2004). Its low detection limit and high spatial resolution of ~1-5 µm makes it the ideal technique to analyze melt inclusions trapped in olivine (e.g. Brounce et al., 2014; Hartley et al., 2017; Kelley and Cottrell, 2009, 2012; Moussallam et al., 2016). Because magmas trapped as melt inclusions in primitive crystals are less affected by secondary processes such as degassing of volatiles and fractional crystallization than external magmas, they provide a unique window into the pre-eruptive conditions of magmas.

However, a recent study by Cottrell et al. (2018) showed that hydrous glasses can be affected by beam-induced oxidation during XANES analysis. According to this study, the iron oxidation state of glasses can be modified as a function of the radiation dose (which they defined as the total photons delivered per square micrometer) used to perform analyses, their water contents and their initial iron oxidation state. They found that the higher the radiation dose and

water content of glasses and the lower their initial $Fe^{3+}/\Sigma Fe$, the higher the over-estimation of their $Fe^{3+}/\Sigma Fe$ ratios.

In this study, $Fe^{3+}/\Sigma Fe$ ratios in olivine-hosted melt inclusions from various arcs, OIB and MORB localities were analyzed by µ-XANES spectroscopy after determination of the analytical conditions that allowed us to mitigate beam damage. In addition, for the first time, the $Fe^{3+}/\Sigma Fe$ ratios of a subset of those melt inclusions were analyzed by synchrotron Mössbauer source spectroscopy. The $Fe^{3+}/\Sigma Fe$ ratios obtained with these two methods on the same sample set allow us to constrain the oxidation state of iron in those magmas by avoiding the effect of beam-induced oxidation that may occur during XANES analysis. Then we were able to confirm that arc magmas are more oxidized than those from hot spots and mid-ocean ridges. Our results suggest that the variation in the oxidation state observed in our melt inclusion dataset may be linked to changes in the oxidation state of the mantle beneath arcs due to subduction processes.

2. Natural samples

Secondary processes such as magmatic differentiation and degassing of volatile species can affect magmas during their ascent to the surface and modify their chemical composition and their oxidation state (e.g. Cottrell and Kelley, 2011; Kelley and Cottrell, 2012; Moussallam et al., 2016). To investigate the oxidation state of primitive magmas, we selected melt inclusions trapped in high-Mg olivines (i.e., with a forsterite content > 80%). We selected primary melt inclusions that were far from any crack, did not display daughter minerals or devitrification and therefore did not require re-homogenization. The 33 studied melt inclusions are larger than 30 µm and most of them contain a bubble that most likely formed after entrapment (Figure 1 of the Supplementary material).

We selected glassy melt inclusions from a picritic lapilli layer collected on the Torgil tuff ring and from the Red Cliff pyroclastic sequence (Ao15, Ao17, Ao2T-T, Ao-T; Sorbadere et *al.*, 2011) of Aoba volcano in the Vanuatu arc. Melt inclusions from Mont Etna were selected from the FS marker bed located on its eastern flank, and formed during a subplinian picritic eruption dated at 3930 ± 60 BP (SVP291c; Coltelli et al., 2005; Kamenetsky et al., 2007). We also selected melt inclusions from scoria samples from the ~50 000 year old La Sommata pyroclastic cone on Vulcano Island (Som; Rose-Koga et al., 2012), and from a tephra layer located in a trench dug at 450 m a.s.l. on the northeastern flank of Stromboli volcano (St82p; Métrich et al., 2001; Rosi et al., 2000) in the Aeolian arc. Melt inclusions were selected from a Pleistocene-aged tephra layer from the mosaic ridge in the Mount Meager Volcanic Complex in the Garibaldi volcanic belt in the Cascades volcanic arc (Aw-15-185; Venugopal et al., in prep). Previously studied melt inclusions from a picritic scoria sample from Piton de Caille on the Northwest rift-zone of Piton de la Fournaise, Reunion Island (CAI; Bureau et *al.*, 1998a; Bureau et *al.*, 1998b; Laubier, 2006) and from mid-ocean ridge basalts from the FAMOUS zone (Northern Mid-Atlantic Ridge; ARP73-10-03; Kamenetsky, 1996; Laubier et al., 2007, 2012) and the Gakkel ridge are also part of our dataset.

3. Experimental samples

A series of 14 basaltic glasses were synthetized experimentally and used as reference material for XANES measurements. The starting composition was a MORB glass collected in the axial rift of the Pacific mid-ocean ridge (Searise 1 DR 04; Latitude 6.71, Longitude -114.30 and depth = 2800 m). The sample was ground under ethanol in an agate mortar to a homogeneous powder mixture.

Experiments under anhydrous conditions at 0.1 MPa (ML1 to 9) were performed at Laboratoire Magmas et Volcans (Clermont-Ferrand, France) in a vertical quenching furnace, with a CO_2–H_2 gas atmosphere. The oxygen fugacity was monitored using a ZrO_2–CaO oxygen cell calibrated against the Fe-FeO, Ni-NiO and Cu-Cu_2O buffers. In order to cover a range of redox conditions, experiments were performed at different fO_2 conditions ranging from -3,5 log units below the quartz–fayalite–magnetite buffer (QFM-3.5) to QFM+4. The sample material for these experiments consisted of ~ 50-70 mg of the mixture that had been mixed with polyvinyl alcohol and pressed into a pellet. This pellet was then sintered onto an iron–platinum alloy loop, which had been previously annealed with the starting composition in order to prevent Fe loss to the alloy during the experiment. The run temperature was continuously monitored using a Pt–$Pt_{90}Rh_{10}$ thermocouple. The thermocouple was placed in the hotspot of the furnace, where the thermal gradient is <1°C over the length of the sample. The sample was suspended alongside the thermocouple in order to minimize the difference between the temperature of the sample and the reading of the thermocouple. The reproducibility and measurement of this arrangement is better than 5°C. The experiments were run isothermally at 1350 °C at the run conditions and typically for 24h.

The BH hydrous glasses (BH1, BH3, BH6 BH7 and BH10) were synthesized at Laboratoire Magmas et Volcans in a piston-cylinder apparatus at 1 GPa and 1300 °C using a 1/2" assembly. The starting materials consisted of anhydrous glasses that were first synthesized by re-melting the starting material in a gas-mixing furnace at one bar, 1350 °C and three different fO_2 conditions of ~QFM, QFM+2 and QFM+4. The glasses were then ground under ethanol in an agate mortar to a homogeneous powder mixture. For the piston-cylinder experiments, we used a Pyrex-MgO assembly, a graphite heater, an outer NaCl sleeve, and Au_{80}-Pd_{20} capsules (with a 4 mm outer diameter for 1/2″ assemblies, 0.2 mm wall thickness, 4–5 mm length). To prepare the capsules, we first added deionized water at the bottom of the

capsule using a micro-syringe. After loading and compacting ~50 mg of glass powder, the capsule was welded shut. We checked for leaks during capsule preparation by weighing the welded capsules before and after ≥ 1h heating at 120 °C in an oven. Before starting the experiments, the capsules were placed in an oven at 120 °C overnight to ensure homogenous distribution of the volatiles. During the experiments, the samples were held at 1300 °C and 1 GPa for only 15 min in order to minimize fO_2 re-equilibration and H_2O loss. The temperature was measured very close to the capsule by a $W_{95}Re_5$-$W_{74}Re_{26}$ thermocouple. Quenching of the hydration experiments was done by switching off the heating power, which led to a cooling rate > 80 °C/s.

The glasses recovered from the experiments were polished on both sides for major element characterization by electron microprobe, H_2O concentration measurements by Raman spectroscopy (for hydrous glasses only) and XANES measurements. Fragments of the anhydrous glasses were also analyzed by conventional Mössbauer spectroscopy using a radioactive point source at the Bayerisches Geoinstitüt. Details of the experimental conditions for each run, as well as their chemical compositions can be found in Table 1-2 of the Supplementary material.

Three basaltic and three basanitic experimental glasses from Magnien et al. (2004) and Schiavi et al. (2018), respectively, were added to our dataset to complete the range of $Fe^{3+}/\Sigma Fe$ ratios and water contents covered by our experimental glasses. Their chemical compositions can be found in Tables 1-2 of the Supplementary material.

4. Analytical methods

4.1.Electron microprobe analyzes

Melt inclusions and their host olivines were analyzed for major elements by electron microprobe at Laboratoire Magmas et Volcans with a CAMECA SX 100. All analyzes were performed with a 15 kV accelerating voltage. Olivines were measured with a 1 µm diameter focused beam and a 100 nA beam current. Counting times for each element were: Al (160-220 s), Si (20 s), Mg (30 s), Ca (160 s), Fe (40 s), Mn (60 s) and Ni (120 s). Analyzes of Si, Mg and Fe of olivines presenting a slightly tilted surface were performed in EDS mode using the electron microprobe to avoid bias on their stoichiometry. Counting time for these three elements using this analytical condition was 30 s. Melt inclusions were analyzed with a 10 µm diameter beam and two beam current conditions. The elements measured with a 8 nA beam and their respective counting times were: Na (10 s), Mg (30 s), Si (10 s), Al (20 s), Ca (10 s), Ti (30 s) and Fe (30 s). The elements measured at 50 nA and the respective counting times were: K (40 s), P (40 s) and Mn (80 s). Volatile elements were analyzed with a 10 µm diameter beam and a beam current of 40 nA. Respective counting times were: S (50 s), Cl (50 s) and F (300 s). Analytical uncertainties on glass data for major elements were obtained from replicate measurements on the natural glass Ve32 (n = 23). The total analytical 2σ error, which corresponds to the maximum value between the precision and accuracy of measurements, for the Ve32 basaltic glass was 1.4% rel. for SiO_2, 4.1% for TiO_2, 2.8% for Al_2O_3, 4.8% for FeO*, 11% for MnO, 3.4% for MgO, 3.2% for CaO, 9.2% for Na_2O, 9.9% for K_2O and 4.6% for P_2O_5. The major and volatile element compositions of melt inclusions and the major element compositions of their host crystals are given in Table 3 of the Supplementary material. The values on the Ve32 standard are also reported in Table 3 of the Supplementary material.

4.2.Raman spectroscopy

Water content of 14 melt inclusions was determined by Raman spectroscopy. Spectra were collected at Laboratoire Magmas et Volcans using an InVia (Renishaw) confocal Raman micro-spectrometer. Analytical details can be found in Schiavi et al. (2018). The diode laser output power was 150 mW. Laser power on the sample was reduced by filters in order to operate at powers of ~ 1 mW. Laser power on the sample was periodically checked. The analytical conditions used result in lateral and axial spatial resolutions of ~1 and 3 μm, respectively, near the sample surface. Daily calibration of the spectrometer was performed based on a Si 520.5 cm^{-1} peak. Analyzes were carried out at 2 μm depth on polished melt inclusions. The spectra were recorded in the wavenumber ranges from ~100 to 1350 cm^{-1} (alumino-silicate network domain) for 4 cycles of 30 s and from ~2900 to 3800 cm^{-1} (water domain) for 7 cycles of 30 s, using Wire 4.2 software. Basaltic, andesitic and rhyolitic glasses, with water content from 0 to 6.70 ± 0.35 wt% were used as external reference standards (Médard and Grove, 2008; Schiavi et al., 2018) and analyzed several times during each analytical session at the same conditions as the samples, in order to correct for the dependence of band intensities on delivered energy. Analytical precision calculated based on repeated daily measurements of the reference glass 82-72f#9 was better than 16 % rel. Analyzes of host olivines were performed with the same conditions in order to correct melt inclusion spectra that suffered from signal contamination from the host crystal.

Absolute intensity areas of the water band and silicate band were determined after subtraction of a cubic and non-parametric baseline, respectively, using PeakFit© software. For determination of water content in glasses, we used both the external calibration procedure, which is based on the absolute intensities of the water band area, and an internal calibration procedure which normalizes the intensity of the water band area to the area of the silicate bands (Schiavi et al., 2018). The two methods often gave different results (up to ~30% rel.). As

demonstrated by Schiavi et al., (2018), the internal calibration is sensitive to matrix effects that are related to changes in glass density, the oxidation state or the presence of dissolved carbonate. For those reasons, we used an external calibration to determine the water content of our melt inclusions. The analytical uncertainty was calculated as the 2σ relative standard deviation (RSD) on replicate measurements. When melt inclusions could only be analyzed once, we report an analytical uncertainty that corresponds to the maximal 2σ RSD determined on replicate analyzes of other melt inclusions in the same session. Water contents of melt inclusions are given in Table 3 of the Supplementary material.

4.3.FTIR spectroscopy

The water contents of 16 melt inclusions were determined by Fourier Transform infrared spectroscopy. Analyzes were performed at LMV using a Bruker Vertex 70 spectrometer coupled with a Hyperion microscope. The spectrometer is equipped with a Globar light source, a KBr beamsplitter and a Mercury-Cadmium-Tellurium alloy (MCT) detector. Melt inclusions polished on both sides were placed on a CaF_2 window for the acquisition and the CaF_2 window was used for background correction. The beam size varied as a function of the melt inclusion size. Absorbance and background spectra were obtained by acquisition of 600 and 300 scans, respectively. The spectral resolution was 4 cm^{-1}. Spectra were collected in the wavenumber range from 7500 to 700 cm^{-1}. Spectra were corrected for atmospheric contamination using OPUS software. The water contents of melt inclusions were calculated using the Beer-Lambert law. Absorption was derived from the area of the 3550 cm^{-1} band after baseline subtraction using OPUS software. Sample thicknesses were measured as the vertical displacement of the optical microscope stage between the top of the sample and the sample holder using a focused Raman laser beam. The uncertainty on the thickness measurement was estimated to be ~2 µm. The density was calculated following Bouhifd et al. (2015). For basaltic glasses, we used a

molar absorption coefficient of 62.8 ± 0.8 $Lmol^{-1}cm^{-1}$ as proposed by Mercier et al. (2010). For silicate under-saturated samples, we chose to use a molar absorption coefficient of 43.96 ± 0.6 $Lmol^{-1}cm^{-1}$ (Mercier et al., 2010). The analytical uncertainty was calculated as the 2σ relative standard deviation (RSD) on replicate measurements. When melt inclusions could only be analyzed once, we report an analytical uncertainty that corresponds to the maximal 2σ RSD determined on replicate analyzes of other melt inclusions in the same session. Water contents of melt inclusions are given in Table 3 of the Supplementary material.

A few melt inclusions were both analyzed by Raman and FTIR spectroscopy. From the comparison between the two methods, we concluded that both methods gave consistent results, but that the uncertainties on the water contents derived from FTIR spectroscopy were larger due to the error on the thickness of melt inclusions and the uncertainty resulting from the range in the published values for the molar absorption coefficient. Therefore, when both types of data were available, the water contents derived from Raman spectroscopy were preferentially used.

4.4.Mössbauer analyzes

The iron speciation of the 12 anhydrous experimental glasses (Table 1 of the Supplementary material) was determined by conventional Mössbauer spectroscopy. Analyzes were carried out at the Bayerisches Geoinstitut, Bayreuth. Glasses were mounted between two pieces of plastic film and centered in a 1000 µm diameter hole drilled in a 25 µm thick Pb foil. Data were collected in transmission mode on a constant acceleration Mössbauer spectrometer with a nominal 370 MBq ^{57}Co point source in a 12 µm Rh matrix with active dimension of 500 × 500 μm^2. The velocity scale was calibrated with a 25 µm thick natural α-Fe foil. A line width of 0.36 mm/s for the outer lines was obtained for α-Fe at room temperature. Analyzes were performed at room temperature with measuring times from 7 hours to 5 days.

$Fe^{3+}/\Sigma Fe$ in 14 olivine-hosted melt inclusions were determined using a synchrotron Mössbauer source (SMS; Potapkin et al., 2012; Smirnov et al., 1997). Analyzes were carried out at the Nuclear Resonance beamline ID18 (Rüffer and Chumakov, 1996) of the European Synchrotron Facility, Grenoble. Melt inclusions were polished on both sides to avoid signal contamination from their host crystal and were centered under a 20-30 µm hole drilled in a 25 µm-thick Re foil. Data were collected using a multi-bunch operating mode and a 10 × 15 μm^2 focalized beam for 4.5 to 9 hours at room temperature. The SMS provided ^{57}Fe resonant radiation with the energy of 14.4125 keV and the bandwidth of ~13 neV tunable in the energy range of about ± 0.3 µeV. The velocity scale was calibrated with a 25 µm-thick natural α-Fe foil and the source line width was checked after each analysis. Spectra were fitted using MossA software using a full transmission integral (Prescher et al., 2012).

The fitting methods applied to spectra collected using conventional Mössbauer and SMS spectroscopy are further described in the Results section.

4.5.XANES analyzes

Fe K-edge X-ray absorption near edge structure (XANES) were collected at the LUCIA (Vantelon et al., 2016) beamline of SOLEIL synchrotron, France, during five different sessions in 2014, 2015, 2017, 2018 and 2019. Data were collected in fluorescence mode between 7050 and 7300 eV, with 0.1 eV steps in the pre-edge region (7106–7120 eV). The excitation energy was selected using a Si(311) or a Si(111) double crystal monochromator depending on the analytical session, leading to a spectral energy resolution of 0.2 and 1 eV, respectively. The monochromator was calibrated by setting the first inflexion point of a Fe metallic foil to 7112 eV. The beam was focused using KB mirrors down to ~ 3 × 3 μm^2 (Table 4 of the Supplementary material). The fluorescence detector was a Bruker silicon drift diode mono-element with a total active area of 60 mm^2. The distance between the sample and the detector

was adjusted to ensure optimal counting rate for each sample. Samples were tilted at an angle of 5° with respect to the incident beam. X-ray fluorescence (XRF) chemical maps were used to select spots for XANES measurements. Spectra collected in anhydrous reference glasses during each session were used to refine the alignment of the spectra collected during the different cessions and to calibrate $Fe^{3+}/\Sigma Fe$ ratios obtained from the pre-edge region of XANES spectra collected on our unknown samples. For unknown samples, two consecutive XANES spectra were collected at the same location. More details on the analytical conditions are given in Tables 4-5 of the Supplementary material.

Cottrell et al. (2018) demonstrated that hydrous glasses can be affected by beam-induced oxidation depending on their H_2O content, their initial oxidation state and the radiation dose used to collect spectra. Therefore, during our 2019 session, we acquired XANES spectra on hydrous glasses using different radiation doses ranging from 7.9×10^5 to 2.4×10^8 photons/s/µm². This was done by changing the beam size from 3.7 × 3 to 35 × 15 μm^2 and/or attenuating the beam flux by placing a 60 µm thick Al foil along the beam path (Tables 4-5 of the Supplementary material). The radiation dose corresponds to the number of photons delivered to the sample per square micrometer. The sample area exposed to radiation was determined assuming that the beam had an elliptic shape. Melt inclusions were then analyzed during that 2019 session with a 4 × 3 μm^2 focused beam size using radiation doses of 3.7×10^7 photons/s/µm².

To better constrain conditions at which beam-induced oxidation occurs, we tested for a time dependent variation in the intensity of the pre-edge multiplets. Following Debret et al. (2015) and Cottrell et al. (2018), we measured the peak amplitude at two fixed energies that correspond to the energies of the Fe^{2+} and Fe^{3+} pre-edge peaks, respectively (7112.6 and 7114 eV), during 300 s. The duration of a time series acquisition corresponds to the time needed to

collect the pre-edge part of our XANES spectra. The time series were acquired at the same conditions as the XANES spectra (Tables 4-5 of the Supplementary material).

XANES spectra were normalized and corrected for self-absorption using Athena software (IFFEFIT suite; Ravel et Newville, 2005). Melt inclusion spectra were tested for potential contamination from the host olivine crystal by carrying out a comparison with spectra collected on synthetic glasses and using the principal component analysis procedure described in Hartley et al. (2017) and Shorttle et al. (2015). The $Fe^{3+}/\Sigma Fe$ ratios of samples were derived by fitting the pre-edge region using PeakFit© software. The pre-edge region was fitted between 7108 and ~7118 eV with two Gaussian peaks, constrained to have the same width and line shape, simultaneously with the background, which was modeled as the tail of two other Gaussian functions. The pre-edge centroid energies, integrated areas and intensity ratios calculated as $I_{Fe^{3+}}/(I_{Fe^{3+}} + I_{Fe^{2+}})$ are reported in Table 6 of the Supplementary material. Intensities collected as a function of time at 7112.6 and 7114 eV in the same sample were normalized as $I[(Fe^{3+})/[I(Fe^{3+})+I(Fe^{2+})]] = I(7114)/[I(7114)+I(7112.6)]$ in order to track the evolution of the $Fe^{3+}/\Sigma Fe$ ratios through time.

5. Results

5.1.Mössbauer spectroscopy

5.1.1. Independent characterization of the $Fe^{3+}/\Sigma Fe$ ratios in reference glasses

Several methods were tested to fit the Mössbauer spectra (e.g. Berry et al., 2018; Cottrell et al., 2009) in order to define the best fitting method to apply to our data. The best fit as judged

by statistics and consistency of parameters across all spectra for reference glasses was obtained with three pseudo-Voigt doublets (Figure 1).

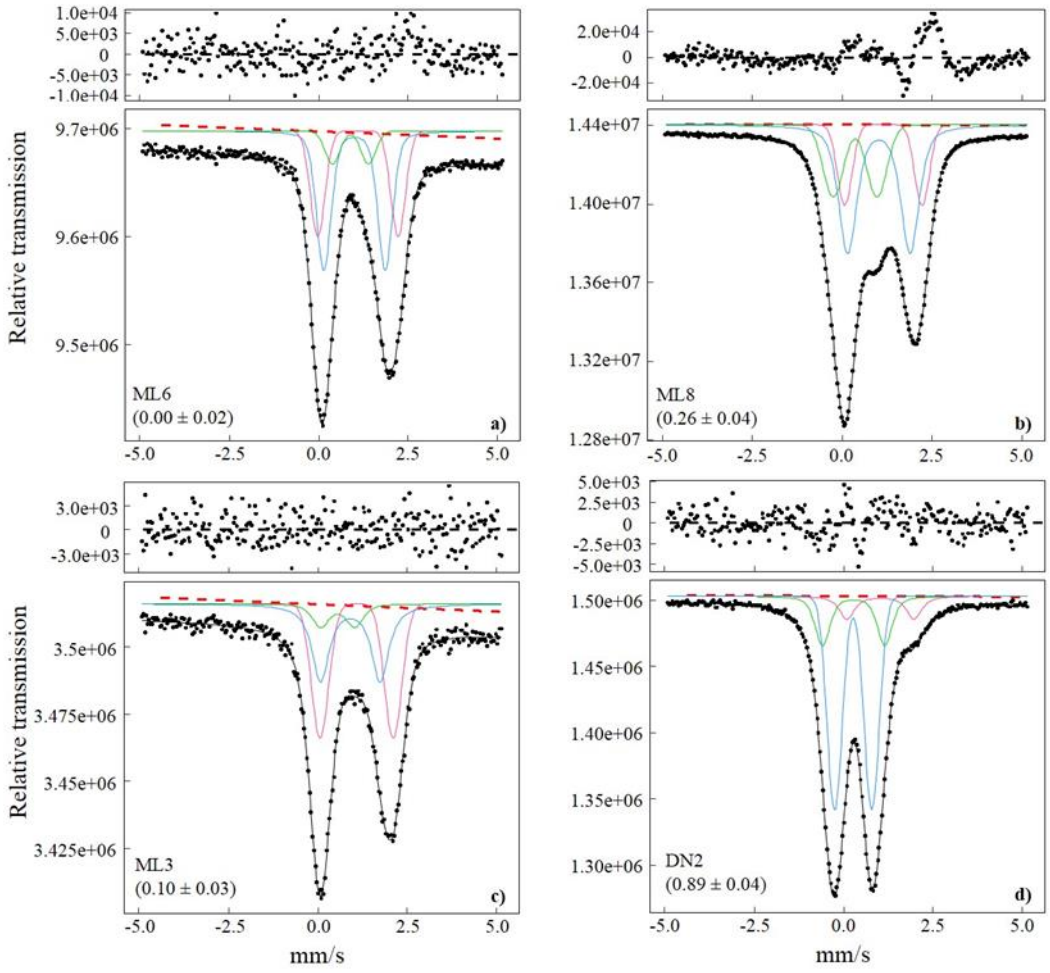

Figure 1: Results of the fitting procedure of four Mössbauer spectra collected for anhydrous basaltic reference glasses (Table 1 of the Supplementary material). The $Fe^{3+}/\Sigma Fe$ ratios of the glasses are given in brackets. The red dashed line corresponds to the linear baseline. The black line represents the modeled spectra. Blue, green and pink lines correspond to the three pseudo-Voigt doublets used to characterize iron environments. For the most reduced glasses (a) the three doublets are attributed to the Fe^{2+} environment. For reduced and oxidized glasses (b-c), the green pseudo-Voigt doublet was attributed to the Fe^{3+} environment whereas the two others were attributed to the Fe^{2+} environment. For the more oxidized sample (d), the pink pseudo-

339 Voigt doublet was attributed to the Fe^{2+} environment whereas the two others were attributed to
340 the Fe^{3+} environment. Residuals obtained from the fitting procedure are given at the top of the
341 spectra.
342
343 The values for the center shift (δ), quadrupole splitting (Δ) and the full width at half
344 maximum (FWHM) for each doublet were set as free to vary at first. Then, the FWHMs of the
345 three doublets were constrained to be equal when unrealistic values were obtained for hyperfine
346 parameters. Reduced χ^2 values range from 0.95 to 1.93. Values obtained for hyperfine
347 parameters are summarized in Table 7 of the Supplementary material. The values obtained for
348 the hyperfine parameters indicate that two doublets are attributed to the Fe^{3+} environment,
349 whereas one doublet is attributed to the Fe^{2+} environment in our most oxidized glass. In contrast,
350 two doublets are attributed to the Fe^{2+} environment and one doublet is attributed to the Fe^{3+}
351 environment in the less oxidized glasses. Three doublets are attributed to the Fe^{2+} environment
352 in our most reduced glasses (e.g. Alberto et al., 1996; Berry et al., 2018; Cottrell et al., 2009;
353 Zhang et al., 2018); Table 7 of the Supplementary material). $Fe^{3+}/\Sigma Fe$ ratios were obtained from
354 the relative area of each doublet. Determination of the 2σ uncertainty is based on both the
355 statistical uncertainty derived from the fit and the reproducibility given by results obtained from
356 the several tested methods. The fit results are reported in Table 7 and Figure 1.
357 The values obtained for the hyperfine parameters in our most reduced glass standards
358 suggest that no Fe^{3+} component is required. However, the doublets are characterized by broad
359 lines and the hyperfine parameters show a systematic overlap of the Fe^{2+} components that
360 suggests that a small amount of Fe^{3+} could be present in these reference glasses (Figure 1a).
361 Therefore, we conclude that we are not able to determine the iron speciation accurately in
362 glasses with < 10 % $Fe^{3+}/\Sigma Fe$, and for that reason we decided not to use those in our XANES
363 calibration (Table 1 of the Supplementary material).

5.1.2. $Fe^{3+}/\Sigma Fe$ in melt inclusions

Due to a limited beamtime, synchrotron Mössbauer source spectra collected on melt inclusions have a lower signal to noise ratio than conventional Mössbauer spectra in the reference glasses (Figure1-2). The consequence of this lower signal quality is that we were not able to apply the same fitting method for melt inclusions and reference glasses (Figure 2). However, in order to be as consistent as possible with the fitting procedure used for reference glasses, spectra collected on melt inclusions were fitted using two pseudo-Voigt doublets, where one doublet was attributed to the Fe^{2+} environment and the other one was attributed to the Fe^{3+} environment. As for reference glasses, hyperfine parameters (δ and Δ) and the FWHM of the doublets were first set as free to vary. Then, the FWHM of the doublets attributable to the Fe^{3+} environment was fixed to 0.4 mm/s when unrealistic values were obtained for hyperfine parameters. An asymmetric Lorentzian doublet with fixed hyperfine parameters was added to the fitting procedure (Figure 2) to correct the spectra for ^{57}Fe contamination from the Be lenses. Reduced χ^2 values range from 0.86 to 1.15. Hyperfine parameters are summarized in Table 8 of the Supplementary material.

Since the ^{57}Fe contamination due to the Be lenses is larger for spectra collected on iron-poor or thin melt inclusions, we tested for a correlation between the relative area of the Lorentzian doublet from the Be lenses and the Mössbauer thickness of the different samples (Table 9 and Figure 2 of the Supplementary material). The Mössbauer thickness is calculated from the density (g/cm^3), porosity (%), thickness (µm) and total iron content (in wt% of element) of the sample (Long et al., 1983). The broad negative trend follows the expected behavior of the two parameters, i.e. the area of the Lorentzian doublet increases as either the iron content or the sample thickness decreases, confirming our approach to correct for ^{57}Fe contamination by the Be lenses.

$Fe^{3+}/\Sigma Fe$ ratios were derived from the relative areas of each doublet and 2σ uncertainties were calculated from the statistical fitting uncertainties reported by the software. Results are shown in Table 3 of the Supplementary material.

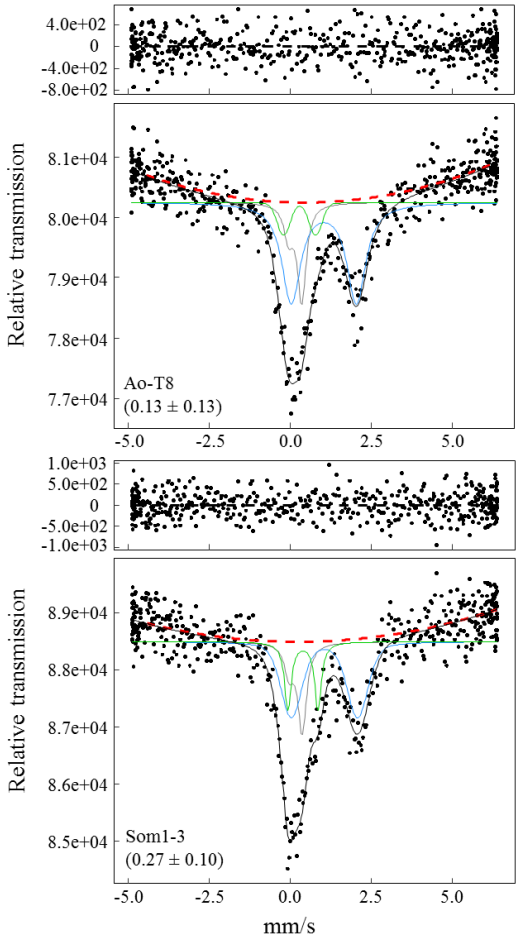

Figure 2: Results of the fitting procedure applied to two room temperature Mössbauer spectra collected on melt inclusions using the synchrotron Mössbauer source. The $Fe^{3+}/\Sigma Fe$ ratios of selected melt inclusions are given in brackets. The red dashed line corresponds to the quadratic baseline. The black line represents the modeled spectra. The grey line is the Lorentzian doublet used to correct spectra for ^{57}Fe contamination from the Be lenses. Blue and green lines are the pseudo-Voigt doublets attributed to the Fe^{2+} and Fe^{3+} environments, respectively. Residuals obtained after the fitting procedure are given at the top of the spectra.

5.2.XANES

5.2.1. Calibration of the XANES spectra

To derive $Fe^{3+}/\Sigma Fe$ ratios from the pre-edge region of XANES spectra collected on unknown samples, these spectra have to be calibrated using XANES spectra collected on reference glasses with independently known $Fe^{3+}/\Sigma Fe$ ratios (e.g. derived from Mössbauer spectroscopy). In previous studies, the XANES calibration uses either the pre-edge centroid energy (i.e., intensity-weighted energy) or the pre-edge intensity ratio (i.e., the ratio of the total area of the Fe^{3+} peak [$I(Fe^{3+})$] to the sum of the areas of the Fe^{3+} peak [$I(Fe^{3+})$] and the Fe^{2+} peak [$I(Fe^{2+})$], or $I(Fe^{3+})/[I(Fe^{3+})+I(Fe^{2+})]$). Pre-edge centroid energy-based calibrations are less sensitive to changes in the coordination environment (Berry et al., 2003; Wilke et al., 2004), however they are more sensitive to energy shifts that can occur during and between analytical sessions (Cottrell et al., 2009). As spectra were collected on the same reference glasses during every session, we were able to correct our spectra for any shift in energy between sessions (no drift occurred within single sessions). Therefore, we applied the pre-edge centroid energy based calibration to estimate the $Fe^{3+}/\Sigma Fe$ ratios in the unknown samples.

Cottrell et al. (2009) also used a pre-edge centroid energy based calibration and found that the use of a second order polynomial fit to their most oxidized reference glasses was appropriate for their data. The use of this calibration leads to the determination of an average $Fe^{3+}/\Sigma Fe$ ratio of 0.16 ± 0.01 for MORB glasses (Cottrell and Kelley, 2011). More recently, Berry et al. (2018) proposed that a linear calibration can be used to determine $Fe^{3+}/\Sigma Fe$ of MORB glasses when only considering the appropriate $Fe^{3+}/\Sigma Fe$ range for MORBs ($Fe^{3+}/\Sigma Fe < 0.3$). They derived an average $Fe^{3+}/\Sigma Fe$ ratio of 0.11 ± 0.02 for MORB glasses when they use the linear calibration and 0.10 ± 0.02 when they use the polynomial calibration. Results derived from these two calibrations are similar within error, which indicates that both calibrations can

425 be applied to determine $Fe^{3+}/\Sigma Fe$ ratios in the unknown samples. These authors have also
426 proposed that the difference in the average $Fe^{3+}/\Sigma Fe$ ratio in MORB glasses arises from the
427 method applied to fit the Mössbauer spectra of reference glasses. On the one hand, Cottrell et
428 al. (2009) fitted their Mössbauer spectra using two 2D-gaussian doublets, with one doublet
429 being attributed to the Fe^{2+} environment and the other one to the Fe^{3+} environment. On the other
430 hand, Berry et al. (2018) have proposed that a third doublet has to be attributed to the Fe^{2+}
431 environment, in particular in the case of reduced samples, otherwise their $Fe^{3+}/\Sigma Fe$ would be
432 over-estimated. In the current study, we used three doublets to fit the Mössbauer spectra
433 collected on our reference glasses and the third doublet was attributed to the Fe^{2+} environment
434 in our most reduced samples, therefore we expect that our derived $Fe^{3+}/\Sigma Fe$ ratios are not over-
435 estimated.

436 $Fe^{3+}/\Sigma Fe$ ratios derived from XANES spectra were determined for our natural glass
437 samples from the centroid energy of the fitted pre-edge region using a polynomial calibration
438 derived from seven basaltic reference glasses (Figure 3; Table 1 of the Supplementary material).
439 As the $Fe^{3+}/\Sigma Fe$ ratios of our more reduced standards are below the detection limit of Mössbauer
440 spectroscopy (<10 %), we did not use them in our calibration (Table 1 of the Supplementary
441 material).

442 The XANES calibration is given by the equation:

443

444 $$E_{centroid} = -1.0540\ (Fe^{3+}/\Sigma Fe)_{Mössbauer}{}^{2} + 2.6146\,(Fe^{3+}/\Sigma Fe)_{Mössbauer} +$$

445 $$7\,112.8004 \qquad (1)$$

446

447 in which $E_{centroid}$ corresponds to the centroid energy (in eV) and $(Fe^{3+}/\Sigma Fe)_{Mössbauer}$ is the
448 $Fe^{3+}/\Sigma Fe$ value obtained by Mössbauer spectroscopy. This calibration is applicable to samples
449 with $Fe^{3+}/\Sigma Fe$ ratios ranging between 0.10 and 0.90. The accuracy of the calibration was tested

by using one of our anhydrous experimental glasses (ML4; Table 1 of the Supplementary material) as an external standard. The mean $Fe^{3+}/\Sigma Fe$ ratio of 0.22 ± 0.02 (n=6) calculated for the ML4 glass using this calibration is in good agreement with the $Fe^{3+}/\Sigma Fe$ of 0.21 ± 0.03 obtained by Mössbauer spectroscopy. This result demonstrates that our calibration can be used to determine $Fe^{3+}/\Sigma Fe$ ratios of our unknown samples. The uncertainty on the ML4 glass is reported as the 2σ standard deviation of the replicate analyzes. This uncertainty will then be used as the 2σ error on the $Fe^{3+}/\Sigma Fe$ ratios of our unknown samples.

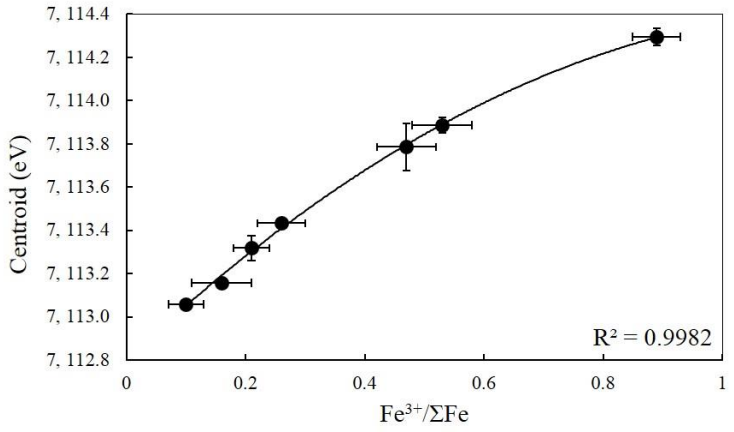

Figure 3: XANES calibration curve for the determination of the $Fe^{3+}/\Sigma Fe$ ratios of melt inclusions and glasses. The solid curve is the second order polynomial fit result. Averaged centroid energies and $Fe^{3+}/\Sigma Fe$ ratios from Mössbauer spectroscopy of anhydrous basaltic reference glasses are shown in Table 1 of the supplementary material. Error bars are reported as 2σ uncertainties (Table 1 of the supplementary material).

5.2.2. Time series in hydrous synthetic glasses

The measurement of the evolution of the pre-edge peak intensities with time at fixed energies gives us access to the evolution of the iron speciation of glasses during the time required to acquire the XANES pre-edge region, which, in our set-up, is about 5 minutes. The time series allows us to spot the occurrence of beam damage during acquisition. Time series

collected on hydrous experimental glasses with water contents ranging from 0.02 ± 0.002 to 2.86 ± 0.34 wt% and equilibrated at various fO_2 show no clear evidence of beam damage when using radiation doses lower than 1.2×10^8 photons/s/µm². When using higher doses, the time series collected on water-rich glasses (≥ 2.48 ± 0.20 wt% H_2O) show a systematic increase in the intensity ratio I(7114)/[I(7114)+I(7112.6)] (Figure 4). As time series are collected at fixed energies, the effect of beam-induced oxidation cannot be monitored using centroid positions. However, when considering a XANES spectrum, the use of the centroid position allows us to determine more accurate $Fe^{3+}/\Sigma Fe$ ratios.

At 2.4×10^8 photons/s/µm², time series collected on the BH1 glass (0.74 ± 0.02 wt% H_2O) also show an increase in its intensity. This suggests that beam damage can even occur for very low water contents when using such high radiation doses.

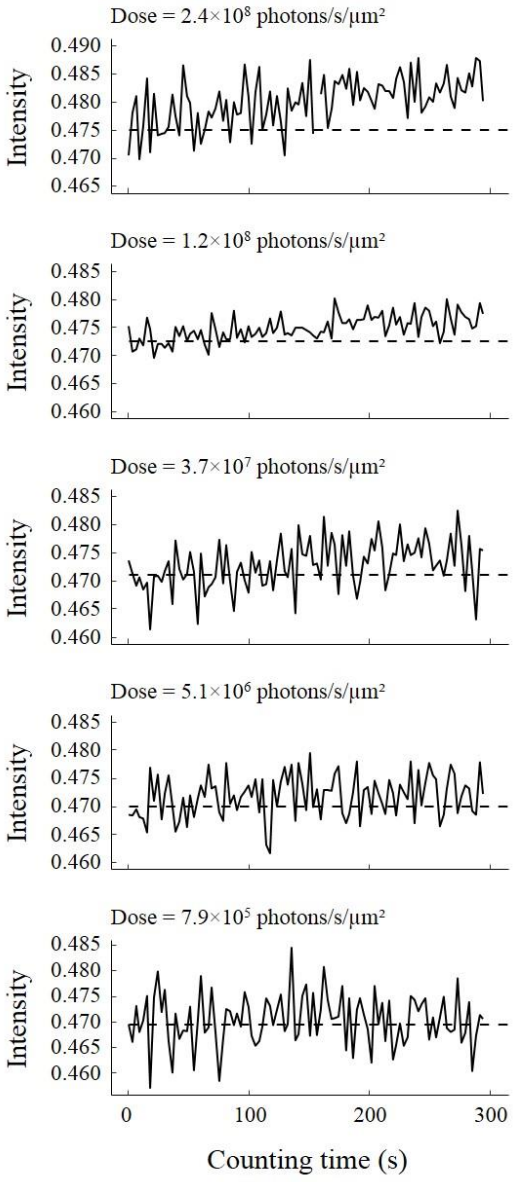

Figure 4: Time series of the intensity ratio I(7114)/[I(7114)+I(7112.6)] collected over 300 s in the most hydrous experimental glass BSN101117 - 2 (Table 2 of the Supplementary material) using radiation doses from 7.9×10^5 to 2.4×10^8 photons/s/µm². No evidence of beam damage is visible when using radiation doses lower than 1.2×10^8 photons/s/µm². When using higher radiation doses ($\geq 1.2 \times 10^8$ photons/s/µm²) beam damage effects are recorded as an increase in the intensity through time. The overestimation of the $Fe^{3+}/\Sigma Fe$ calculated from these time series is 10% rel. and 15% rel. using 1.2×10^8 and 2.4×10^8 photons/s/µm² respectively.

We converted the intensity of absorption recorded in the time series into $Fe^{3+}/\Sigma Fe$ ratios using a calibration based on non-normalized pre-edge peak intensity ratios in the reference glasses. Then we applied a linear regression through the variation of $Fe^{3+}/\Sigma Fe$ with time to calculate the over-estimation of $Fe^{3+}/\Sigma Fe$ induced by beam damage. We find that $Fe^{3+}/\Sigma Fe$ ratios are over-estimated by 6 to 10 % rel. and 6 to 15 % rel. when using radiation doses of 1.2×10^8 and 2.4×10^8 photons/s/µm², respectively. The percentage of over-estimation of the $Fe^{3+}/\Sigma Fe$ ratios shows a poor positive correlation with the water content of glasses (Figure 5a) and no correlation with their original $Fe^{3+}/\Sigma Fe$ ratios (i.e., as determined from the pre-edge centroid energy of a spectrum collected in non-damaging conditions (5.1×10^6 photons/s/µm²; Figure 5b). Cottrell et al. (2018) found that the beam damage susceptibility φ, which they define as the product of the water concentration and the ferrous/ferric oxide ratio on a molar basis, is positively correlated with the percentage of over-estimation of $Fe^{3+}/\Sigma Fe$ ratios recorded for hydrous glasses. Our data do not show such correlation (Figure 5c). The lack of correlation between these parameters implies that we were not able to quantify the over-estimation of $Fe^{3+}/\Sigma Fe$ ratios for glasses analyzed using standard radiation doses (~10^8 photons/s/µm²) and for which time series have not been collected.

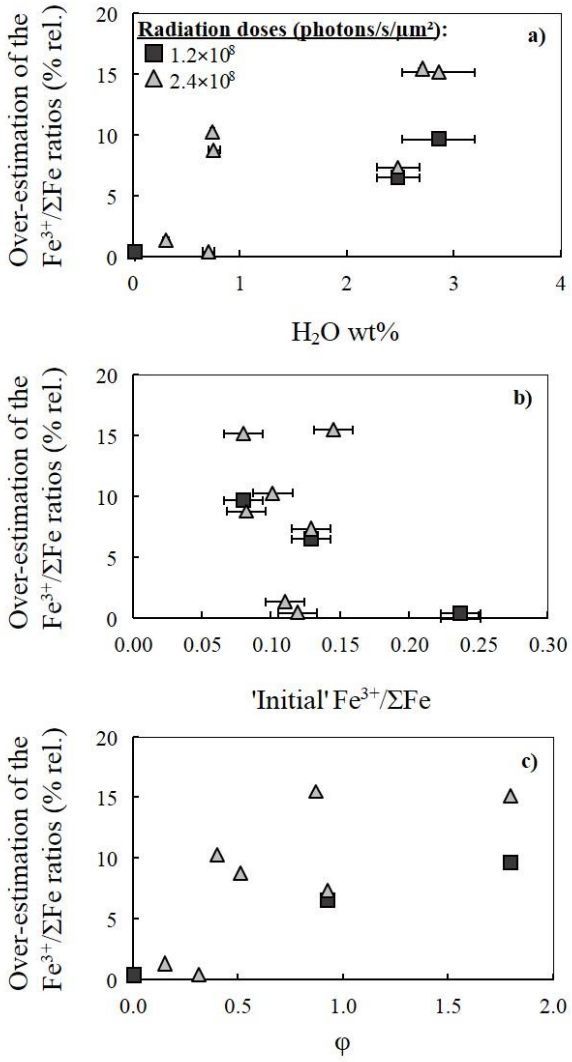

Figure 5: Overestimation of the $Fe^{3+}/\Sigma Fe$ ratios recorded by time series collected in hydrous glasses as a function of (a) their water content, (b) their 'initial' $Fe^{3+}/\Sigma Fe$ ratios determined in non-photo-oxidizing conditions (5.1×10^6 photons/s/µm²) and (c) the beam damage susceptibility φ ($\varphi = XHO_{0.5} \times XFeO/XFeO_{1.5}$; Cottrell et al., 2018). Squares and triangles represent the overestimation of $Fe^{3+}/\Sigma Fe$ ratios recorded for radiation doses of 1.2×10^8 and 2.4×10^8 photons/s/µm², respectively. Errors given on water contents and 'initial' $Fe^{3+}/\Sigma Fe$ ratios are expressed as 2σ errors (Table 2 of the Supplementary material).

5.2.3. XANES spectra in hydrous synthetic glasses

We first compared the pre-edge features of XANES spectra successively collected at the same location in our synthetic hydrous glasses to look for evidence for beam-induced oxidation between the two consecutive spectra (Figure 6). Changes in the pre-edge feature indicating that beam damage occurred during the acquisition were visible for water-rich glasses ($\geq 2.48 \pm 0.20$ wt% H_2O) that were analyzed with radiation doses of 1.2×10^8 and 2.4×10^8 photons/s/µm². When we compared the $Fe^{3+}/\Sigma Fe$ ratios obtained for these spectra, the over-estimation of the $Fe^{3+}/\Sigma Fe$ ratios derived from the second spectrum is systematically contained in the 2σ uncertainty on these ratios. Similarly, we compared the $Fe^{3+}/\Sigma Fe$ ratios obtained for these spectra with their original $Fe^{3+}/\Sigma Fe$ ratios (i.e., as determined from the pre-edge centroid energy of a spectrum collected in non-damaging conditions of 5.1×10^6 photons/s/µm²). The over-estimation of $Fe^{3+}/\Sigma Fe$ derived from XANES spectra that were affected by beam damage (as evidenced by time series and modification of the pre-edge region of XANES spectra) lies within the error except for BH7 at the highest radiation dose. We can also note that all the glasses that show changes in the pre-edge feature between two consecutive spectra also show evidence of beam induced oxidation in the time series. However, the inverse is not systematically observed (and this might indicate that the photo-oxidation has reached a plateau and/or that it is irreversible).

When no beam damage was detected either from the time series and/or the comparison of the pre-edge regions of the two consecutive spectra, we calculated a mean $Fe^{3+}/\Sigma Fe$ from the two spectra collected at the same spot. 2σ uncertainties were calculated as the propagation of the 2σ uncertainty of the $Fe^{3+}/\Sigma Fe$ ratios of both spectra. On the other hand, when there was evidence for oxidation from the difference in the two spectra, we discarded the value from the second spectrum and only kept the $Fe^{3+}/\Sigma Fe$ ratio derived from the first spectrum.

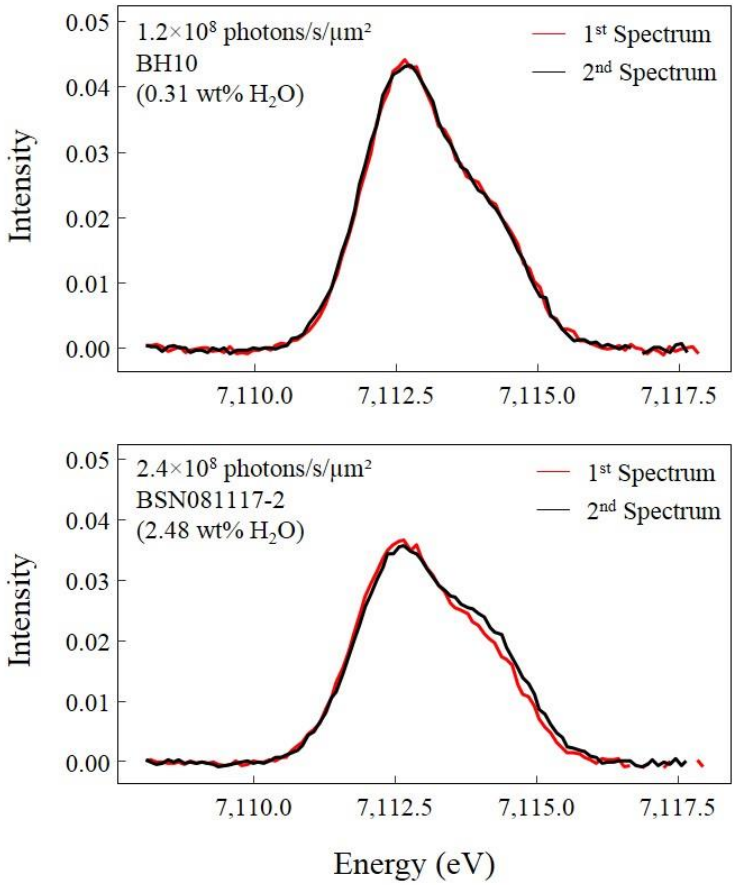

Figure 6: Pre-edge regions after baseline subtraction of two successive XANES spectra collected at the same spot. The spectra shown here were collected in hydrous glasses BH10 and BSN081117 - 2 (their water contents are given in brackets; Table 2 of the Supplementary material) with radiation doses of 1.2×10^8 and 2.4×10^8 photons/s/μm², respectively. The first and second spectra are shown in red and black, respectively. The two spectra collected in the BH10 glass are identical. In contrast, the second spectrum collected in the BSN081117 - 2 glass shows a small decrease in its Fe^{2+} component and an increase in its Fe^{3+} component compared to the first spectrum, indicating beam damage.

When using a radiation dose of about 10^7 photons/s/μm², we record no evidence of beam-induced oxidation from the time series and the two consecutive spectra. This indicates that decreasing the radiation dose of about one order of magnitude provides more accurate

549 $Fe^{3+}/\Sigma Fe$ ratios while still keeping the small beam size that is required for melt inclusion
550 analysis.

551 ### 5.2.4. Determination of $Fe^{3+}/\Sigma Fe$ in melt inclusions

552 Time series were collected using a radiation dose of 3.7×10^7 photons/s/µm² in melt
553 inclusions that were large enough to accommodate several XANES spots. As we saw no
554 evidence for beam-induced oxidation in the hydrous experimental glasses at the same beam
555 conditions, we expected no beam damage in the melt inclusions. As expected, we found no
556 evidence for beam damage in the time series of most melt inclusions except for three arc melt
557 inclusions: the relative increase of the $Fe^{3+}/\Sigma Fe$ ratio with time ranges from 6 to 63% rel. for
558 water contents ranging from 2.31 to 4.14 wt% (Table 3 of the Supplementary material). The
559 percentage of over-estimation of the $Fe^{3+}/\Sigma Fe$ ratios does not, however, correlate with the water
560 content in the melt inclusions. One should note that the largest amount of over-estimation of
561 the $Fe^{3+}/\Sigma Fe$ ratio (63% rel.) is comparable or sometimes lower than the 2σ uncertainties
562 attributed to the $Fe^{3+}/\Sigma Fe$ ratios calculated from Mössbauer spectra. However, we have
563 demonstrated that the absolute $Fe^{3+}/\Sigma Fe$ value calculated from the XANES spectrum is biased.
564 In addition to the time series, we also compared the pre-edge features of two spectra that
565 were successively acquired at the same location. Beam damage affecting the second spectrum
566 is clearly visible in eleven water-rich arc melt inclusions with water contents ranging from 2.31
567 to 4.59 wt%. Still, this effect is minimal and only one of them (inclusion SVP291c n4) shows
568 an over-estimation of its $Fe^{3+}/\Sigma Fe$ ratio that is larger than the 2σ uncertainty on the $Fe^{3+}/\Sigma Fe$
569 ratio. Surprisingly this melt inclusion shows no clear evidence for beam damage in the time
570 series, which suggests that the first spectrum has not been affected by beam damage and that
571 the $Fe^{3+}/\Sigma Fe$ ratio derived from it is reliable. In the end, more than half of the water-rich (> 1

572 wt% H_2O) melt inclusions did not show modification of the pre-edge feature between the two
573 consecutive spectra.

574 When no sign of beam damage was recorded in the time series and/or in the comparison
575 of the pre-edge regions of two spectra collected on the same spot, we calculated a mean
576 $Fe^{3+}/\Sigma Fe$ ratio from the two spectra. 2σ uncertainties were calculated as the propagation of the
577 2σ uncertainties of the $Fe^{3+}/\Sigma Fe$ ratios of both spectra. When time series could not be collected
578 for lack of space in the inclusion, we calculated a mean $Fe^{3+}/\Sigma Fe$ ratio from the two spectra
579 when their $Fe^{3+}/\Sigma Fe$ ratios lie within the 2σ errors. Melt inclusions for which time series exhibit
580 evidence of beam damage were removed from our dataset. When melt inclusions have been
581 analyzed in different spots, mean $Fe^{3+}/\Sigma Fe$ ratios were calculated using only the first spectra
582 collected at each spot when the time series didn't record any beam damage. Results are given
583 in Table 3 of the Supplementary material.

584 # 6. Discussion

585 ## 6.1. The effect of beam-induced oxidation on the determination of
586 ## $Fe^{3+}/\Sigma Fe$ ratios in silicate glasses

587 The time series collected on hydrous experimental glasses by XANES indicate that
588 beam damage systematically takes place at high water contents (≥ 2.5 wt% H_2O) for durations
589 of 5 minutes and standard radiation doses (~10^8 photons/s/µm²; Figure 4). At lower water
590 contents (< 1 wt% H_2O), beam damage is not systematically observed. Beam induced oxidation
591 recorded in the time series is usually, but not systematically, supported by changes in the pre-
592 edge feature between the two XANES spectra collected successively at the same location (one
593 spectrum acquisition lasts for 7 to 20 min; Figure 6), which suggests that the oxidation process

continues to occur during acquisition of the second spectrum. To explain the cases where time series showed oxidation through time, but no change was noticeable between the pre-edge features of the two spectra successively collected, we can make two hypotheses. The first hypothesis is that beam damage is "completed" after full acquisition of the pre-edge (Cottrell et al., 2018). The second hypothesis is that the modification due to beam damage is not systematically large enough to be visible given our spectral resolution. The $Fe^{3+}/\Sigma Fe$ ratios calculated for hydrous experimental glasses from their pre-edge centroid energies suggest that the effect of this process may be within the error associated with the calculation of these ratios. However, based on time series, an over-estimation of $Fe^{3+}/\Sigma Fe$ of about 15 % rel. may occur when using a radiation dose of 2.4×10^8 photons/s/µm². Thus, the $Fe^{3+}/\Sigma Fe$ ratios of melt inclusions, and especially of arc melt inclusions that are usually water-rich, will likely be over-estimated when analyzing them with such doses.

A large number of melt inclusions have been analyzed with standard radiation doses (~10^8 photons/s/µm²) during our first synchrotron sessions. At the time, as we did not realize how large the effects of beam damage could be, we did not systematically collect time series. The lack of or the poor correlation between the chemical composition of glasses (in particular their H_2O contents and/or initial $Fe^{3+}/\Sigma Fe$) and the over-estimation of the $Fe^{3+}/\Sigma Fe$ ratios recorded by time series collected on hydrous synthetic glasses (Figure 5) means that we are not able to quantify the over-estimation that potentially affected the $Fe^{3+}/\Sigma Fe$ ratios derived from XANES spectra collected on these melt inclusions using standard beam conditions. Therefore, we were not able to correct them and we decided not to use them.

Time series collected on hydrous experimental glasses using radiation doses lower than ~10^8 photons/s/µm² do not show any evidence for oxidation. However, time series acquired in three hydrous melt inclusions using a radiation dose of 3.7×10^7 photon/s/µm² show evidence of beam damage. Moreover, melt inclusions that exhibit an over-estimation of the $Fe^{3+}/\Sigma Fe$

ratio derived from the second spectrum compared to the first one do not systematically display an evolution of the speciation through time in the time series. These observations corroborate the ones carried out by Cottrell et al. (2018) showing that lowering the radiation dose to about ~10^7 photons/s/µm² allows us to mitigate but not definitively eliminate beam-induced oxidation during XANES analyzes. Using these more appropriate beam conditions, only three melt inclusions out of thirty show clear signs of beam damage during the acquisition of the first pre-edge spectrum.

6.2.$Fe^{3+}/\Sigma Fe$ inferred from Mössbauer vs. XANES spectroscopy

For the first time, the $Fe^{3+}/\Sigma Fe$ ratios of olivine-hosted melt inclusions were determined by Mössbauer spectroscopy. Despite counting times of 4.5 to 9 h, the limited thickness of our melt inclusions resulted in much larger uncertainties in $Fe^{3+}/\Sigma Fe$ than the ones determined for reference glasses using conventional Mössbauer spectroscopy (Tables 1 and 3 of the Supplementary material). The difference can be explained by the lower signal to noise ratio of spectra collected on melt inclusions (Figure 1-2). Furthermore, these uncertainties are even larger for the most reduced melt inclusions ($Fe^{3+}/\Sigma Fe < 0.15$; Figure 3 of the Supplementary material). The increased uncertainties with decreasing $Fe^{3+}/\Sigma Fe$ ratio are explained by decreasing signal to noise ratio with decreasing Fe^{3+} content in the melt inclusions.

Figure 7 shows the comparison between $Fe^{3+}/\Sigma Fe$ ratios obtained by synchrotron Mössbauer source and XANES spectroscopy.

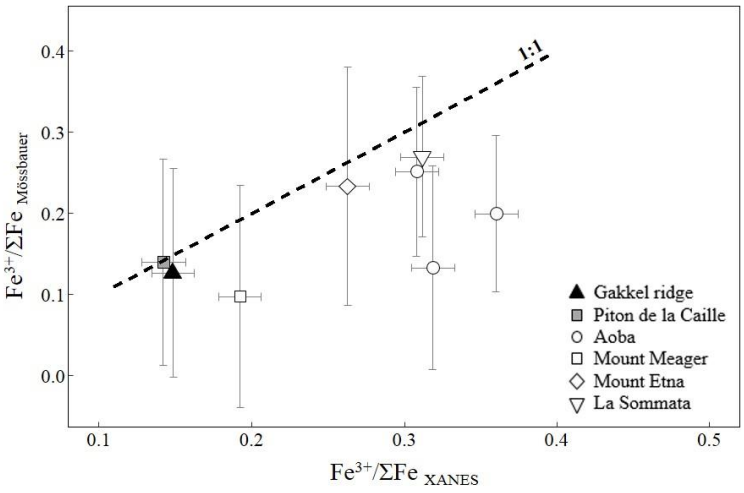

638

639 Figure 7: $Fe^{3+}/\Sigma Fe$ ratios from Mössbauer spectroscopy compared to those from XANES
640 spectroscopy. Here we report data from MORB and OIB melt inclusions from the Gakkel ridge
641 (black triangles) and Piton de la Caille (Reunion island; grey squares), arc melt inclusions from
642 Aoba (empty circles), Mount-Meager (squares), La Sommata (inverted triangles) and melt
643 inclusions from Mount Etna (diamonds). Errors bars are reported as 2σ uncertainties (Table 3
644 of the Supplementary material).

645

646 The figure shows that $Fe^{3+}/\Sigma Fe$ ratios derived from these two methods mostly overlap within
647 the 2σ uncertainties, with a distribution close to the 1:1 line. Nevertheless, we note that the
648 absolute $Fe^{3+}/\Sigma Fe$ values calculated from Mössbauer spectra are generally lower than the ones
649 obtained from XANES. Only two arc melt inclusions from Aoba (inclusions Ao17-D6 and Ao-
650 T8) show significantly lower Mössbauer-derived $Fe^{3+}/\Sigma Fe$. The first hypothesis we can make
651 is that these two melt inclusions were oxidized during XANES analysis. However, we see no
652 evidence for beam-induced oxidation in the time series nor in the comparison of two
653 consecutive spectra. A second hypothesis is that a small proportion of host olivine was sampled
654 by the beam during Mössbauer analyses. The spectra collected in the Ao-T8 melt inclusion do
655 not show evidences of signal contamination from the host olivine (Figure 2). Thus, it is more
656 likely that the $Fe^{3+}/\Sigma Fe$ ratio obtained from Mössbauer spectroscopy in Ao-T8 is

underestimated because of the low signal to noise ratio and increased error. The poor signal to noise ratio of the spectra collected in the Ao17-D6 melt inclusion does not allow us to be as definitive as for the spectra collected in the Ao-T8 melt inclusion (Figure 4 in the supplementary material).

Generally, the comparison of $Fe^{3+}/\Sigma Fe$ ratios inferred from these two methods seems to indicate that we managed to detect beam damage when it occurred during XANES analysis. However, the fact that the $Fe^{3+}/\Sigma Fe$ ratios obtained by Mössbauer spectroscopy exhibit larger uncertainties because of the low spectral resolution indicates that we are not able to determine precise $Fe^{3+}/\Sigma Fe$ ratios using synchrotron Mössbauer yet, unless we increase counting times significantly.

6.3. The oxidation state of melt inclusions

In order to discuss further the oxygen fugacity at which melt inclusions equilibrate, their compositions have to be corrected for post-entrapment modification. Melt inclusions were corrected for host crystallization and/or 'Fe loss' using Petrolog3 software (Danyushevsky and Plechov, 2011). Details on the correction method used in this study are available in the Supplementary material. Corrected compositions and 'original' $Fe^{3+}/\Sigma Fe$ ratios are reported in Table 3 of the Supplementary material.

Our results show that melt inclusions from MORB display a mean $Fe^{3+}/\Sigma Fe$ ratio of 0.10 ± 0.05 (n=5). Melt inclusions from OIB and arcs display mean $Fe^{3+}/\Sigma Fe$ ratios of 0.13 ± 0.05 (n=2) and 0.25 ± 0.15 (n=19) respectively. Mount Etna is not classified as an arc volcano and has a more complex geodynamic setting than the other volcanoes presented in this study. Many authors suggested that Mount Etna has an OIB signature but for which the mantle is metasomatized by subduction-derived fluids. Nevertheless, the composition of the mantle beneath Mount Etna is still debated (e.g. Correale et al., 2014; Schiano et al., 2001; Schiavi et

al., 2015; Tonarini et al., 2001; Viccaro et Zuccarello, 2017). Our results show that melt inclusions collected in our Mount Etna sample display a mean $Fe^{3+}/\Sigma Fe$ ratio of 0.26 ± 0.05 (n=7) that is closer to the mean value obtained for arc melt inclusions than the one obtained for OIB melt inclusions.

In Figure 8, we report the number of melt inclusions as a function of their geodynamic setting (melt inclusions from Mount Etna are reported here as arc melt inclusions) and their calculated $Fe^{3+}/\Sigma Fe$ ratios (light grey). Also reported are previously published data for melt inclusions in high-Mg olivines (> Fo_{80}; dark grey) and glasses (black) from MORBs (Berry et al., 2018; Birner et al., 2018; Cottrell and Kelley, 2011, 2013; Kelley and Cottrell, 2009; Zhang et al., 2018), OIBs (Brounce et al., 2017; De Moor et al., 2013; Hartley et al., 2017; Moussallam et al., 2016) and arcs (Brounce et al., 2014; Kelley and Cottrell, 2009, 2012). This figure shows that the $Fe^{3+}/\Sigma Fe$ ratios in melt inclusions from MORBs are in good agreement with previous data and comparable to the ones obtained by Berry et al. (2018; 0.10 ± 0.02). $Fe^{3+}/\Sigma Fe$ ratios calculated for melt inclusions from OIBs show similar or lower values than the previously published XANES data. This result may indicate beam-induced oxidation or that the range of $Fe^{3+}/\Sigma Fe$ ratios recorded for OIBs is larger than previously reported (Brounce et al., 2017; De Moor et al., 2013; Hartley et al., 2017; Moussallam et al., 2016). Melt inclusions from arcs from this study display a range in $Fe^{3+}/\Sigma Fe$ ratios that is in good agreement with previous data (Brounce et al., 2014; Kelley and Cottrell, 2009, 2012). A few melt inclusions exhibit $Fe^{3+}/\Sigma Fe$ ratios that are higher than literature data. This suggests that the range of oxidation state recorded in arc magmas may be larger than previously observed. Therefore, our results confirm that arc magmas are more oxidized than those from hot spots and mid-ocean ridges.

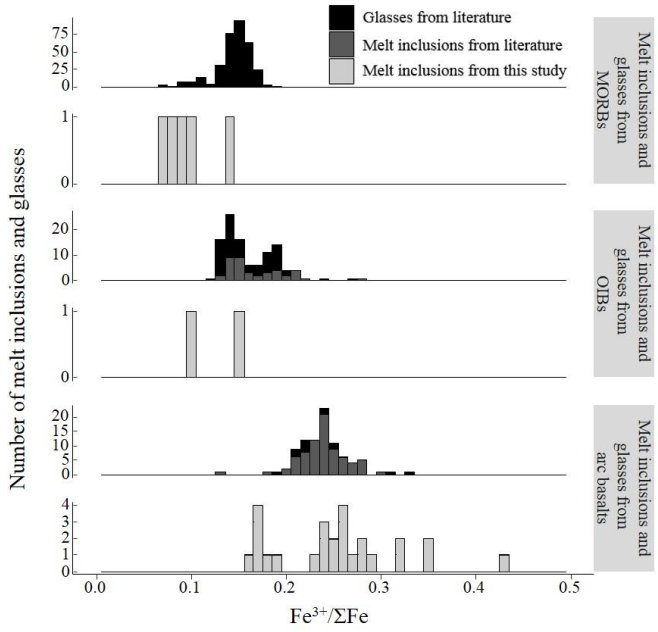

Figure 8: Number of melt inclusions and glasses as a function of their $Fe^{3+}/\Sigma Fe$ ratios and geological settings. $Fe^{3+}/\Sigma Fe$ ratios plotted in this graph are mainly derived from XANES measurements at a radiation dose of 3.7×10^7 photons/s/µm² (light grey; Table 3 of the Supplementary material). When XANES spectra showed evidence of beam damage, we report $Fe^{3+}/\Sigma Fe$ ratios, we report $Fe^{3+}/\Sigma Fe$ ratios derived from Mössbauer spectroscopy instead (6 melt inclusions). Also reported are literature data for glasses (black) and melt inclusions from high-Mg olivines (> Fo_{80}) from arc basalts, OIBs and MORB for comparison (dark grey; Berry et al., 2018; Birner et al., 2018; Brounce et al., 2014, 2017; Cottrell and Kelley, 2011, 2013; De Moor et al., 2013; Hartley et al., 2017; Kelley and Cottrell, 2009, 2012; Moussallam et al., 2016; Zhang et al., 2018).

Similarly observations by Kelley and Cottrell (2009), $Fe^{3+}/\Sigma Fe$ correlates positively with the H_2O content in melt inclusions (Figure 9). These authors suggested that the positive correlation between these two parameters most likely reflects changes in the oxidation state of the mantle beneath arcs because of subduction processes.

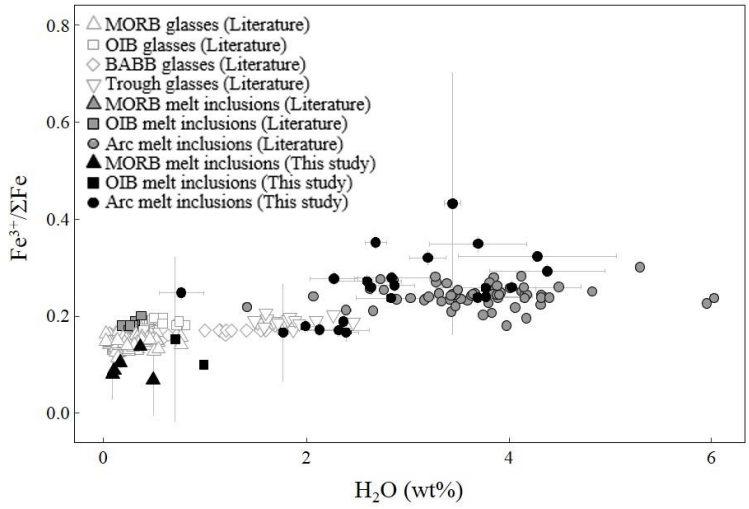

719

720 Figure 9: $Fe^{3+}/\Sigma Fe$ ratios of melt inclusions as a function of their water content. $Fe^{3+}/\Sigma Fe$ ratios
721 reported in this graph are mainly derived from XANES measurements at a radiation dose of
722 3.7×10^7 photons/s/µm² (light grey; Table 3 of the Supplementary material). When XANES
723 spectra showed evidence of beam damage, we report $Fe^{3+}/\Sigma Fe$ ratios, we report $Fe^{3+}/\Sigma Fe$ ratios
724 derived from Mössbauer spectroscopy instead (6 melt inclusions). Data from this study are
725 represented by black symbols. Error bars are 2σ (Table 3 of the Supplementary material).
726 Previous data (grey symbols) from Brounce et al. (2014, 2017), Cottrell and Kelley (2011),
727 Kelley and Cottrell (2009, 2012), Moussallam et al. (2016) and Zhang et al. (2018) collected in
728 glasses and melt inclusions from high-Mg olivines (> Fo_{80}) are also reported.

729

730 fO_2 values of our melt inclusions were calculated relative to the QFM buffer using the
731 algorithm of Kress and Carmichael (1991) and are reported in Table 3 of the Supplementary
732 material and in Figure 9. The QFM values reported in Figure 10 show that melt inclusions from
733 arc basalts are generally more oxidized (QFM +0.1 to +2.8) than those from MORBs (QFM -
734 1.9 to -0.1) and OIBs (QFM -0.8 and +0.3).

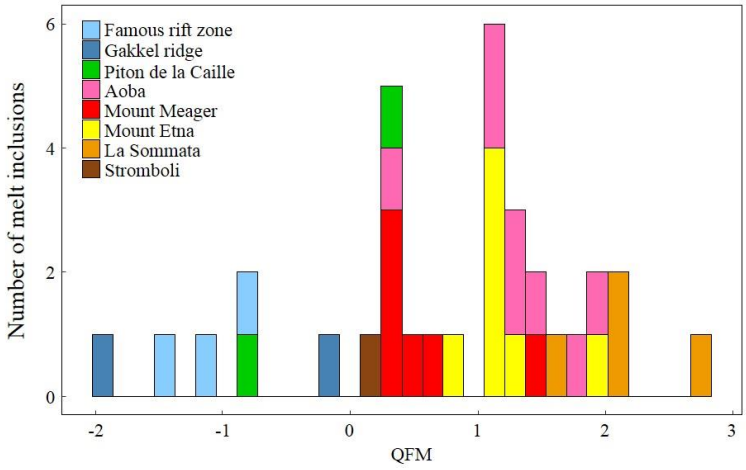

735

736

737 Figure 10: Number of melt inclusions as a function of their fO_2 calculated relative to the QFM
738 buffer using the Kress and Carmichael (1991) algorithm (Table 3 of the Supplementary
739 material). $Fe^{3+}/\Sigma Fe$ ratios plotted in this graph are mainly derived from XANES measurements
740 at a radiation dose of 3.7×10^7 photons/s/µm² (light grey; Table 3 of the Supplementary
741 material). When XANES spectra showed evidence of beam damage, we report $Fe^{3+}/\Sigma Fe$ ratios
742 derived from Mössbauer spectroscopy instead (6 melt inclusions).

743

744 Within our population of melt inclusions from arc basalts, we see a range in fO_2 values. Melt
745 inclusions from Stromboli (Eolian arc) and Mount Meager (Cascades) are the least oxidized
746 with mean fO_2 values of QFM +0.1 and QFM +0.6 (n=6), respectively. Melt inclusions from
747 La Sommata (Vulcano island, Eolian arc) are the most oxidized with a mean fO_2 of QFM +2.1
748 (n=4). Melt inclusions from Aoba volcano (Vanuatu arc) display a mean fO_2 value that is
749 intermediate (QFM +1.3, n=8). Furthermore, we note that melt inclusions from Aoba display
750 the largest range in fO_2, overlapping nearly the entire range in fO_2 in all the arc melt inclusions
751 from this study. Melt inclusions from Mount Etna display a mean fO_2 value of QFM +1.2 (n=7).
752 This fO_2 value is closer to arc values than the OIB values determined in this study.

7. Conclusions

We used XANES and Mössbauer spectroscopy to determine the $Fe^{3+}/\Sigma Fe$ ratios of primitive olivine-hosted melt inclusions from basaltic samples from various volcanic arcs, mid-ocean ridges and hot spots.

First, a careful evaluation of beam damage effects during XANES analysis was carried out by monitoring changes in the pre-edge feature of XANES spectra and intensities variations of time series. Beam induced oxidation recorded in the time series collected in hydrous experimental glasses using standard radiation doses (~10^8 photons/s/µm²) is usually, but not systematically, supported by changes in the pre-edge feature between the two XANES spectra collected successively at the same location. This suggests that the oxidation process continues to occur during acquisition of the second spectrum and may be "completed" after full acquisition of the pre-edge (Cottrell et al., 2018). Our results show that $Fe^{3+}/\Sigma Fe$ ratios in water-rich glasses ($\geq$ 2.5 w% H_2O) are likely to be over-estimated when derived from XANES spectra collected using standard radiation doses (~10^8 photons/s/µm²). The amount of over-estimation of the $Fe^{3+}/\Sigma Fe$ ratios recorded by the time series does not or poorly correlates with the water content, the 'initial' $Fe^{3+}/\Sigma Fe$ ratio or the beam damage susceptibility φ of glasses as defined by Cottrell et al. (2018). Therefore, it is difficult to assess beam damage effects in melt inclusions that were analyzed using standard radiation doses when time series have not been collected. When a lower radiation dose is used ($\leq 3.7 \times 10^7$ photons/s/µm²), we record no evidence of beam damage in hydrous synthetic glasses. However, time series acquired in three hydrous melt inclusions using a radiation dose of 3.7×10^7 photon/s/µm² show evidence of beam damage. Moreover, melt inclusions that exhibit an over-estimation of the $Fe^{3+}/\Sigma Fe$ ratio derived from the second spectrum compared to the first one do not systematically display an evolution of the speciation through time in the time series. Therefore, decreasing the radiation

dose allowed us to mitigate but not definitively avoid beam damage in all melt inclusions. For that reason, systematic acquisition of time series is recommended even at low radiation doses in order to assess beam damage in glasses.

The iron speciation in a subset of melt inclusions was also analyzed using a Mössbauer synchrotron source. The comparison of $Fe^{3+}/\Sigma Fe$ ratios inferred from these two methods suggests that we successfully identified the melt inclusions that suffered from beam damage. However, $Fe^{3+}/\Sigma Fe$ ratios obtained by Mössbauer spectroscopy exhibit large uncertainties because of low signal to noise ratio. A significant increase of counting times (in the order of a day) would lead to a better resolution, but it would decrease the number of samples that can be analyzed during a synchrotron session.

The $Fe^{3+}/\Sigma Fe$ ratios of melt inclusions derived from XANES spectroscopy using a low radiation dose are in good agreement with previously published data. Our results confirm that primitive arc magmas are more oxidized than those from hot spots and mid-ocean ridges. A positive correlation between the $Fe^{3+}/\Sigma Fe$ ratios calculated for melt inclusions and their water contents suggests that the oxidation recorded in primitive arc magmas is likely linked to changes in the oxidation state of the mantle beneath arcs because of subduction processes (Kelley and Cottrell, 2009). The calculation of the fO_2 relative to the QFM buffer confirms that arc melt inclusions and Mount Etna melt inclusions are more oxidized than MORB and OIB melt inclusions. The results also indicate that the range of oxidation state recorded in arc melt inclusions varies from one subduction zone to another.

Acknowledgments

The staff of the LUCIA beamline, Nicolas Trcera and Pierre Lagarde, are thanked for help with data collection, and we acknowledge the European Synchrotron Radiation Facility

for provision of synchrotron radiation facilities at the beamline ID18. Nicolas Cluzel, Jean-Luc Devidal, Franck Pointud, Didier Laporte are warmly thanked for lab assistance. Oliver Shorttle is thanked for sharing his R codes. Massimo Pompilio is thanked for sharing his SVP291c sample. MG was supported by the Région Auvergne (Nouveau chercheur fellowship to ML). This research was founded by the French Government Laboratory of Excellence initiative (ClerVolc LabEx) and the Région Auvergne (Nouveau chercheur fellowship to ML). This is ClerVolc contribution number XXX.

References

Alberto, H. V., Pinto Da Cunha, J. L., Mysen, B. O., Gil, J. M., & Ayres De Campos, N. (1996). Analysis of Mössbauer spectra of silicate glasses using a two-dimensional Gaussian distribution of hyperfine parameters. *Journal of Non-Crystalline Solids*, *194*, 48‑57. https://doi.org/10.1016/0022-3093(95)00463-7

Berry, A. J., Stewart, G. A., O'Neill, H. S. C., Mallmann, G., & Mosselmans, J. F. W. (2018). A re-assessment of the oxidation state of iron in MORB glasses. *Earth and Planetary Science Letters*, *483*, 114‑123. https://doi.org/10.1016/j.epsl.2017.11.032

Berry, J. A., O'Neill, H. S. C., Kasthuri, D., Jayasurya, S., Campbell, S. J., & Foran, G. J. (2003). XANES calibrations for the oxidation state of iron in a silicate glass. *American Mineralogist*, *88*, 967‑977. https://doi.org/https://doi.org/10.2138/am-2003-0704

Bézos, A., & Humler, E. (2005). The Fe3+/ΣFe ratios of MORB glasses and their implications for mantle melting. *Geochimica et Cosmochimica Acta*, *69*(3), 711‑725. https://doi.org/10.1016/j.gca.2004.07.026

Birner, S. K., Cottrell, E., Warren, J. M., Kelley, K. A., & Davis, F. A. (2018). Peridotites and

basalts reveal broad congruence between two independent records of mantle fO2 despite local redox heterogeneity. *Earth and Planetary Science Letters, 494,* 172‐189. https://doi.org/10.1016/j.epsl.2018.04.035

Bouhifd, M. A., Whittington, A. G., & Richet, P. (2015). Densities and volumes of hydrous silicate melts: New measurements and predictions. *Chemical Geology, 418,* 40‐50. https://doi.org/10.1016/j.chemgeo.2015.01.012

Brounce, M., Kelley, K. A., Cottrell, E., & Reagan, M. K. (2015). Temporal evolution of mantle wedge oxygen fugacity during subduction initiation. *Geology, 43*(9), 775‐778. https://doi.org/10.1130/G36742.1

Brounce, M. N., Kelley, K. A., & Cottrell, E. (2014). Variations in Fe3+/PFe of Mariana Arc Basalts and MantleWedge fO2. *Journal of Petrology, 55*(12), 2513‐2536. https://doi.org/10.1093/petrology/egu065

Brounce, M., Stolper, E., & Eiler, J. (2017). Redox variations in Mauna Kea lavas, the oxygen fugacity of the Hawaiian plume, and the role of volcanic gases in Earth's oxygenation. *Proceedings of the National Academy of Sciences of the United States of America, 114*(34), 8997‐9002. https://doi.org/10.1073/pnas.1619527114

Christie, D. M., Carmichael, I. S. E., & Langmuir, C. H. (1986). Oxidation states of mid-ocean ridge basalt glasses. *Earth and Planetary Science Letters, 79,* 397‐411. https://doi.org/10.1016/0012-821X(86)90195-0

Coltelli, M., Del Carlo, P., Pompilio, M., & Vezzoli, L. (2005). Explosive eruption of a picrite: The 3930 BP subplinian eruption of Etna volcano (Italy). *Geophysical Research Letters, 32*(23), 1‐4. https://doi.org/10.1029/2005GL024271

844 Correale, A., Paonita, A., Martelli, M., Rizzo, A., Rotolo, S. G., Corsaro, R. A., & Di Renzo,
845 V. (2014). A two-component mantle source feeding Mt. Etna magmatism: Insights from
846 the geochemistry of primitive magmas. *Lithos*, *184-187*, 243-258.
847 https://doi.org/10.1016/j.lithos.2013.10.038

848 Cottrell, E., & Kelley, K. A. (2011). The oxidation state of Fe in MORB glasses and the
849 oxygen fugacity of the upper mantle. *Earth and Planetary Science Letters*, *305*, 270-
850 282. https://doi.org/10.1016/j.epsl.2011.03.014

851 Cottrell, E., & Kelley, K. A. (2013). Redox heterogeneity in mid-ocean ridge basalts as a
852 function of mantle source. *Science*, *340*, 1314-1317.
853 https://doi.org/10.1126/science.1233299

854 Cottrell, E., Kelley, K. A., Lanzirotti, A., & Fischer, R. A. (2009). High-precision
855 determination of iron oxidation state in silicate glasses using XANES. *Chemical*
856 *Geology*, *268*, 167-179. https://doi.org/10.1016/j.chemgeo.2009.08.008

857 Cottrell, E., Lanzirotti, A., Mysen, B., Birner, S., Kelley, K. A., Botcharnikov, R., …
858 Newville, M. (2018). A Mössbauer-based XANES calibration for hydrous basalt glasses
859 reveals radiation-induced oxidation of Fe. *American Mineralogist*, *103*(4), 489-501.
860 https://doi.org/10.2138/am-2018-6268

861 Danyushevsky, L. V., & Plechov, P. (2011). Petrolog3: Integrated software for modeling
862 crystallization processes. *Geochemistry, Geophysics, Geosystems*, *12*(7).
863 https://doi.org/10.1029/2011GC003516

864 Dauphas, N., Craddock, P. R., Asimow, P. D., Bennett, V. C., Nutman, A. P., & Ohnenstetter,
865 D. (2009). Iron isotopes may reveal the redox conditions of mantle melting from
866 Archean to Present. *Earth and Planetary Science Letters*, *288*(1-2), 255-267.

867 https://doi.org/10.1016/j.epsl.2009.09.029

868 De Moor, J. M., Fischer, T. P., Sharp, Z. D., King, P. L., Wilke, M., Botcharnikov, R. E., …
869 Kelley, K. A. (2013). Sulfur degassing at Erta Ale (Ethiopia) and Masaya (Nicaragua)
870 volcanoes: Implications for degassing processes and oxygen fugacities of basaltic
871 systems. *Geochemistry, Geophysics, Geosystems*, *14*(10), 4076‐4108.
872 https://doi.org/10.1002/ggge.20255

873 Debret, B., Bolfan-Casanova, N., Padrón-Navarta, J. A., Martin-Hernandez, F., Andreani, M.,
874 Garrido, C. J., … Trcera, N. (2015). Redox state of iron during high-pressure serpentinite
875 dehydration. *Contributions to Mineralogy and Petrology*, *169*(4), 1‐18.
876 https://doi.org/10.1007/s00410-015-1130-y

877 Fialin, M., Wagner, C., Métrich, N., Humler, E., Galoisy, L., & Bézos A. (2001). Fe3+/ΣFe
878 vs. FeLα peak energy for minerals and glasses: Recent advances with the elec-tron
879 microprobe. *American Mineralogist*, *86*, 456‐465. https://doi.org/10.2138/am-2001-0409

880 Gaillard, F., Scaillet, B., Pichavant, M., & Iacono-Marziano, G. (2015). The redox
881 geodynamics linking basalts and their mantle sources through space and time. *Chemical*
882 *Geology*, *418*, 217‐233. https://doi.org/10.1016/j.chemgeo.2015.07.030

883 Gale, A., Laubier, M., Escrig, S., & Langmuir, C. H. (2013). Constraints on melting processes
884 and plume-ridge interaction from comprehensive study of the FAMOUS and North
885 Famous segments, Mid-Atlantic Ridge. *Earth and Planetary Science Letters*, *365*, 209‐
886 220. https://doi.org/10.1016/j.epsl.2013.01.022

887 Hartley, M. E., Shorttle, O., Maclennan, J., Moussallam, Y., & Edmonds, M. (2017). Olivine-
888 hosted melt inclusions as an archive of redox heterogeneity in magmatic systems. *Earth*
889 *and Planetary Science Letters*, *479*, 192‐205. https://doi.org/10.1016/j.epsl.2017.09.029

Jayasuriya, K. D., O'Neill, H. S. C., Berry, A. J., & Campbell, S. J. (2004). A Mössbauer study of the oxidation state of Fe in silicate melts. *American Mineralogist, 89*, 1597-1609.

Kamenetsky, V. (1996). Methodology for the study of melt inclusions in Cr-spinel, and implications for parental melts of MORB from FAMOUS area. *Earth and Planetary Science Letters*, *142*(3-4), 479-486. https://doi.org/10.1016/0012-821x(96)00117-3

Kamenetsky, V. S., Pompilio, M., Métrich, N., Sobolev, A. V., Kuzmin, D. V., & Thomas, R. (2007). Arrival of extremely volatile-rich high-Mg magmas changes explosivity of Mount Etna. *Geology*, *35*(3), 255-258. https://doi.org/10.1130/G23163A.1

Kelley, K. A., & Cottrell, E. (2009). Water and the Oxydation State of Subduction Zone Magmas. *Science*, *325*(5940), 605-607. https://doi.org/10.1126/science.1174156

Kelley, K. A., & Cottrell, E. (2012). The influence of magmatic differentiation on the oxidation state of Fe in a basaltic arc magma. *Earth and Planetary Science Letters*, *329-330*, 109-121. https://doi.org/10.1016/j.epsl.2012.02.010

Kress, V. C., & Carmichael, I. S. E. (1991). Mineralogy and Petrology The compressibility of silicate liquids containing Fe203 and the effect of composition, temperature, oxygen fugacity and pressure on their redox states. *Contrib Mineral Petrol*, *108*, 82-92.

Laubier, M., Gale, A., & Langmuir, C. H. (2012). Melting and crustal processes at the FAMOUS segment (mid-atlantic ridge): New insights from olivine-hosted melt inclusions from multiple samples. *Journal of Petrology*, *53*(4), 665-698. https://doi.org/10.1093/petrology/egr075

Laubier, M., Schiano, P., Doucelance, R., Ottolini, L., & Laporte, D. (2007). Olivine-hosted

melt inclusions and melting processes beneath the FAMOUS zone (Mid-Atlantic Ridge). *Chemical Geology*, *240*(1-2), 129-150. https://doi.org/10.1016/j.chemgeo.2007.02.002

Lee, C. T. A., Leeman, W. P., Canil, D., & Li, Z. X. A. (2005). Similar V/Sc systematics in MORB and arc basalts: Implications for the oxygen fugacities of their mantle source regions. *Journal of Petrology*, *46*(11), 2313-2336. https://doi.org/10.1093/petrology/egi056

Lee, C. T. A., Luffi, P., Le Roux, V., Dasgupta, R., Albaréde, F., & Leeman, W. P. (2010). The redox state of arc mantle using Zn/Fe systematics. *Nature*, *468*, 681-685. https://doi.org/10.1038/nature09617

Li, A. Z. X., & Lee, A. C. T. (2004). The constancy of upper mantle fO2 through time inferred from V/Sc ratios in basalts. *Earth and Planetary Science Letters*, *228*, 483-493. https://doi.org/10.1016/j.epsl.2004.10.006

Long, G. J., Cranshaw, T. E., & Longworth, G. (1983). The ideal Mössbauer effect absorber thickness. *Mössbauer Effect Reference and Data Journal*, *6*(2), 42-49.

Magnien, V., Neuville, D. R., Cormier, L., Mysen, B. O., Briois, V., Belin, S., … Richet, P. (2004). Kinetics of iron oxidation in silicate melts: A preliminary XANES study. *Chemical Geology*, *213*(1-3), 253-263. https://doi.org/10.1016/j.chemgeo.2004.08.047

Mallmann, G., & O'Neill, H. S. C. (2009). The crystal/melt partitioning of V during mantle melting as a function of oxygen fugacity compared with some other elements (Al, P, Ca, Sc, Ti, Cr, Fe, Ga, Y, Zr and Nb). *Journal of Petrology*, *50*(9), 1765-1794. https://doi.org/10.1093/petrology/egp053

Mccammon, C. A. (2004). Mössbauer spectroscopy: Applications. In A. Beran & E.

934 Libowtzky (Éd.), *Spectroscopic methods in mineralogy* (p. 662). Budapest: Eötvös
935 Uiversity Press.

936 Médard, E., & Grove, T. L. (2008). The effect of H2O on the olivine liquidus of basaltic
937 melts: Experiments and thermodynamic models. *Contributions to Mineralogy and*
938 *Petrology*, *155*(4), 417‑432. https://doi.org/10.1007/s00410-007-0250-4

939 Mercier, M., Muro, A. Di, Métrich, N., Giordano, D., Belhadj, O., & Mandeville, C. W.
940 (2010). Spectroscopic analysis (FTIR, Raman) of water in mafic and intermediate glasses
941 and glass inclusions. *Geochimica et Cosmochimica Acta*, *74*(19), 5641‑5656.
942 https://doi.org/10.1016/j.gca.2010.06.020

943 Métrich, N., Bertagnini, A., Landi, P., & Rosi, M. (2001). Crystallization driven by
944 decompression and water loss at Stromboli volcano (Aeolian Islands, Italy). *Journal of*
945 *Petrology*, *42*(8), 1471‑1490. https://doi.org/10.1093/petrology/42.8.1471

946 Moussallam, Y., Edmonds, M., Scaillet, B., Peters, N., Gennaro, E., Sides, I., &
947 Oppenheimer, C. (2016). The impact of degassing on the oxidation state of basaltic
948 magmas: A case study of Kīlauea volcano. *Earth and Planetary Science Letters*, *450*,
949 317‑325. https://doi.org/10.1016/j.epsl.2016.06.031

950 O'Neill, H. S. C., Berry, A. J., & Mallmann, G. (2018). The oxidation state of iron in Mid-
951 Ocean Ridge Basaltic (MORB) glasses: Implications for their petrogenesis and oxygen
952 fugacities. *Earth and Planetary Science Letters*, *504*, 152‑162.
953 https://doi.org/10.1016/j.epsl.2018.10.002

954 Partzsch, G. M., Lattard, D., & McCammon, C. (2004). Mössbauer spectroscopic
955 determination of Fe3+/Fe2+in synthetic basaltic glass: A test of empirical fO2equations
956 under superliquidus and subliquidus conditions. *Contributions to Mineralogy and*

957 *Petrology*, *147*, 565‐580. https://doi.org/10.1007/s00410-004-0571-5

958 Potapkin, V., Chumakov, A. I., Smirnov, G. V., Celse, J. P., Rüffer, R., McCammon, C., &
959 Dubrovinsky, L. (2012). The 57Fe Synchrotron Mössbauer Source at the ESRF. *Journal*
960 *of Synchrotron Radiation*, *19*, 559‐569. https://doi.org/10.1107/S0909049512015579

961 Prescher, C., McCammon, C., & Dubrovinsky, L. (2012). MossA: A program for analyzing
962 energy-domain Mössbauer spectra from conventional and synchrotron sources. *Journal*
963 *of Applied Crystallography*, *45*, 329‐331. https://doi.org/10.1107/S0021889812004979

964 Ravel, B., & Newville, M. (2005). ATHENA, ARTEMIS, HEPHAESTUS: data analysis for
965 X-ray absorption spectroscopy using IFEFFIT. *Journal of Synchrotron Radiation*, *12*,
966 537‐541. https://doi.org/doi:10.1107/S0909049505012719

967 Rose-Koga, E. F., Koga, K. T., Schiano, P., Le Voyer, M., Shimizu, N., Whitehouse, M. J., &
968 Clocchiatti, R. (2012). Mantle source heterogeneity for South Tyrrhenian magmas
969 revealed by Pb isotopes and halogen contents of olivine-hosted melt inclusions.
970 *Chemical Geology*, *334*, 266‐279. https://doi.org/10.1016/j.chemgeo.2012.10.033

971 Rosi, M., Bertagnini, A., & Landi, P. (2000). Onset of the persistent activity at Stromboli
972 Volcano (Italy). *Bulletin of Volcanology*, *62*, 294‐300.
973 https://doi.org/10.1007/s004450000098

974 Rüffer, R., & Chumakov, A. I. (1996). Nuclear-resonance beamline at ESRF. *Il Nuovo*
975 *Cimento D*, *97/98*, 589‐604. https://doi.org/10.1007/BF02458921

976 Schiano, P., Clocchiatti, R., Ottolini, L., & Busa, T. (2001). Transition of Mount Etna lavas
977 from a mantle-plume to an island-arc magmatic source. *Nature*, *412*, 900‐904.

978 Schiavi, F., Bolfan-Casanova, N., Withers, A. C., Médard, E., Laumonier, M., Laporte, D., …

Gómez-Ulla, A. (2018). Water quantification in silicate glasses by Raman spectroscopy: Correcting for the effects of confocality, density and ferric iron. *Chemical Geology*, *483*, 312‑331. https://doi.org/10.1016/j.chemgeo.2018.02.036

Schiavi, F., Rosciglione, A., Kitagawa, H., Kobayashi, K., Nakamura, E., Nuccio, P. M., … Vannucci, R. (2015, juillet 1). Geochemical heterogeneities in magma beneath Mount Etna recorded by 2001-2006 melt inclusions. *Geochemistry, Geophysics, Geosystems*. Blackwell Publishing Ltd. https://doi.org/10.1002/2015GC005786

Shorttle, O., Moussallam, Y., Hartley, M. E., Maclennan, J., Edmonds, M., & Murton, B. J. (2015). Fe-XANES analyses of Reykjanes Ridge basalts: Implications for oceanic crust's role in the solid Earth oxygen cycle. *Earth and Planetary Science Letters*, *427*, 272‑285. https://doi.org/10.1016/j.epsl.2015.07.017

Smirnov, G. V, Van Bürck, U., Chumakov, A. I., Baron, A. Q. R., & Rüffer, R. (1997). Synchrotron Mössbauer source. *Physical Review B*, *55*(9), 5811.

Sorbadere, F., Schiano, P., Métrich, N., & Garaebiti, E. (2011). Insights into the origin of primitive silica-undersaturated arc magmas of Aoba volcano (Vanuatu arc). *Contributions to Mineralogy and Petrology*, *162*, 995‑1009. https://doi.org/10.1007/s00410-011-0636-1

Tonarini, S., Armienti, P., D'orazio, M., & Innocenti, F. (2001). Subduction-like fuids in the genesis of Mt. Etna magmas: evidence from boron isotopes and fuid mobile elements. *Earth and Planetary Science Letters*, *192*, 471‑483. Consulté à l'adresse www.elsevier.com/locate/epsl

Vantelon, D., Trcera, N., Roy, D., Moreno, T., Mailly, D., Guilet, S., … Flank, A. M. (2016). The LUCIA beamline at SOLEIL. *Journal of Synchrotron Radiation*, *23*(2), 635‑640.

https://doi.org/10.1107/S1600577516000746

Viccaro, M., & Zuccarello, F. (2017). Mantle ingredients for making the fingerprint of Etna alkaline magmas: implications for shallow partial melting within the complex geodynamic framework of Eastern Sicily. *Journal of Geodynamics, 109*, 10‐23. https://doi.org/10.1016/j.jog.2017.06.002

Wilke, M., Partzsch, G. M., Bernhardt, R., & Lattard, D. (2004). Determination of the iron oxidation state in basaltic glasses using XANES at the K-edge. *Chemical Geology, 213*(1‐3), 71‐87. https://doi.org/10.1016/j.chemgeo.2004.08.034

Zhang, C., Almeev, R. R., Hughes, E. C., Borisov, A. A., Wolff, E. P., Höfer, H. E., … Koepke, J. (2018). Electron microprobe technique for the determination of iron oxidation state in silicate glasses. *American Mineralogist*, *103*(9), 1445‐1454. https://doi.org/10.2138/am-2018-6437

Zhang, H. L., Cottrell, E., Solheid, P. A., Kelley, K. A., & Hirschmann, M. M. (2018). Determination of Fe3 +/ΣFe of XANES basaltic glass standards by Mössbauer spectroscopy and its application to the oxidation state of iron in MORB. *Chemical Geology*, *479*, 166‐175. https://doi.org/10.1016/j.chemgeo.2018.01.006